SI APPENDIX

Laser- and Cryogenic-Probe-Assisted NMR Enables Hypersensitive Analysis of Biomolecules at Sub-Micromolar Concentration

Yusuke Okuno, Miranda F. Mecha, Hanming Yang, Lingchao Zhu, Charles G. Fry and Silvia Cavagnero*

Department of Chemistry, University of Wisconsin - Madison, 1101 University Ave.,
Madison, Wisconsin, 53706, USA

Correspondence should be addressed to S.C. (Email: cavagnero@chem.wisc.edu, Phone: 608-262-5430).

1. Supplementary Results

1.1. Theoretical prediction of steady-state photo-CIDNP polarization. In a photo-CIDNP experiment, the theoretically predicted steady-state nuclear spin polarization of the k_{th} nucleus of interest ($P_{\%,k}^{\mathrm{M,SS}}$) can be expressed as[1]

$$P_{\%,k}^{\mathrm{M,SS}} = 100\% \times \frac{\mathrm{T}_1^{\mathrm{M}}}{\mathrm{T}_1^{\mathrm{M}^{\bullet+}}} \left(\frac{k_{et}^{\mathrm{eff}}[{}^{\mathrm{T}_1}\mathrm{D}^{\mathrm{SS}}][\mathrm{M}^{\mathrm{SS}}]\left(1+\gamma\right)\xi^{\mathrm{G}}\Phi_{\mathrm{G}}}{k_{ter}^{\mathrm{eff}}[\mathrm{D}^{\bullet-,\mathrm{SS}}] + \frac{1}{\mathrm{T}_1^{\mathrm{M}^{\bullet+}}} + k_{\mathrm{de}}[\mathrm{M}^{\mathrm{SS}}]} \right) / [\mathrm{M}]_o \quad , \tag{S1}$$

where γ is defined as

$$\gamma = \left(\frac{\xi^{\mathrm{F}}\left(1-\Phi_{\mathrm{G}}\right)}{\xi^{\mathrm{G}}\Phi_{\mathrm{G}}} \right) \quad , \tag{S2}$$

with ξ_k^{F} and ξ_k^{G} denoting the normalized probability differences to generate a recombination product in the α and β spin states of the k^th^ nucleus per F-pair and per geminate recombination event, respectively. The parameter Φ_{G} indicates the total probability of geminate recombination per geminate radical pair. In essence, the symbol γ in equation S2 denotes the ratio of polarizations due to F-pair and geminate recombination. The initial and steady-state concentrations of the molecule of interest are $[\mathrm{M}]_0$ and $[\mathrm{M}^{SS}]$, respectively. The symbols $[{}^{\mathrm{T}_1}\mathrm{D}^{\mathrm{SS}}]$ and $[\mathrm{D}^{\bullet-,\mathrm{SS}}]$ denote the steady-state concentrations of the dye in the triplet excited-state and radical form, respectively, and k_{ter}^{eff} is the composite rate constant for the regeneration of M, taking into account all the elementary steps leading to it starting from the free-radical form of the molecule of interest $\mathrm{M}^{\bullet+}$ [1, 2]. The effective rate constant for the bimolecular collision followed by electron transfer between the molecule of interest M and the triplet excited-state dye ${}^{\mathrm{T}_1}\mathrm{D}$ is denoted as k_{et}^{eff}. The degenerate electron exchange rate constant is k_{de}, Finally, $\mathrm{T}_1^{\mathrm{M}}$ and $\mathrm{T}_1^{\mathrm{M}^{\bullet+}}$ are the spin-lattice nuclear relaxation times of the kth nucleus in M and $M^{\bullet+}$, respectively. For Trp, we determined that a 0.2 s irradiation time is sufficient to achieve steady-state nuclear spin polarization.

At very low sample concentration, (e.g., when $[M]_o < 1$ μM), one can consider typical numerical values for $T_1^{M^{\bullet+}}$, k_{ter}^{eff} and k_{de} ($T_1^{M^{\bullet+}} \sim 10^{-4}$ s, $k_{ter}^{eff} \sim 10^{9}$ $M^{-1}s^{-1}$, $k_{de} \sim 10^{8} M^{-1}s^{-1}$)^2, and deduce that

$$1/T_1^{M^{\bullet+}} >> k_{ter}^{eff}[M^{\bullet+,SS}] + k_{de}[M^{SS}] \quad . \tag{S3}$$

Under these conditions, the steady-state normalized nuclear polarization (see relation S1) becomes

$$P_{\%,k}^{M,SS} \approx 100\% \times \frac{T_1^{M}}{T_1^{M^{\bullet+}}} \left(\frac{k_{et}^{eff}[{}^{T_1}D^{SS}][M^{SS}](1+\gamma)\xi^{G}\Phi_{G}}{\frac{1}{T_1^{M^{\bullet+}}}} \right) / [M]_o$$

$$= \frac{T_1^{M} k_{et}^{eff}[{}^{T1}D^{SS}][M^{SS}](1+\gamma)\xi^{G}\Phi_{G}}{[M]_o} \quad . \tag{S4}$$

At this juncture, the following two limiting cases can be considered. First, when the steady-state triplet state dye concentration is much lower than the sample concentration (i.e., $[{}^{T_1}D^{SS}] << [M]_o$), one has that

$$[M^{SS}] \approx [M]_o \quad . \tag{S5}$$

Substitution of relation S4 into S3 leads to

$$P_{\%,k}^{SS} \approx T_1^{M} k_{et}^{eff}[{}^{T_1}D^{SS}](1+\gamma)\xi^{G}\Phi_{G} \times 100\% \quad . \tag{S6}$$

Hence, steady-state nuclear spin polarization is directly proportional to $[{}^{T1}D^{SS}]$ under these conditions.

Alternatively, when the steady-state triplet state dye concentration is much higher than the sample concentration (i.e., $[{}^{T1}D^{SS}] >> [M]_o$), it can be shown (see Appendix) that the concentration of the diamagnetic molecule of interest can be approximated to

$$[M^{SS}] \approx \left(k_{ter}^{eff} / k_{et}^{eff}\right)\left([M]_o\right)^2 / [{}^{T_1}D^{SS}] \times 100\% \quad . \tag{S7}$$

Substitution of relation S6 into S3 yields

$$P_{\%,k}^{\mathrm{SS}} \approx \frac{\left\{\mathrm{T}_1^{\mathrm{M}}\mathrm{k}_{et}^{\mathrm{eff}}[{}^{\mathrm{T_1}}\mathrm{D}^{\mathrm{SS}}]\left(k_{ter}^{\mathrm{eff}}\ /\ k_{et}^{eff}\right)\left([\mathrm{M}]_o\right)^2/[{}^{\mathrm{T_1}}\mathrm{D}^{\mathrm{SS}}]\right\}(1+\gamma)\xi^{\mathrm{G}}\Phi_{\mathrm{G}}}{[\mathrm{M}]_o}\times 100\%$$

$$= \mathrm{T}_1^{\mathrm{M}}k_{ter}^{\mathrm{eff}}[\mathrm{M}]_o(1+\gamma)\xi^{\mathrm{G}}\Phi_{\mathrm{G}}\times 100\% \quad . \qquad \text{(S8)}$$

This interesting result suggests that the nuclear spin polarization is independent of the triplet-state dye population $[{}^{\mathrm{T_1}}\mathrm{D}^{\mathrm{SS}}]$ at very low NMR sample concentration, i.e., when the $[{}^{\mathrm{T1}}\mathrm{D}^{\mathrm{SS}}]>>[\mathrm{M}]_o$ inequality holds. In other words, variations in $[{}^{\mathrm{T_1}}\mathrm{D}^{\mathrm{SS}}]$ are not expected to yield changes in the extent of nuclear spin polarization. In addition, relation S8 shows that at very low sample concentration and in the presence of excess dye the nuclear spin polarization depends on k_{ter}^{eff} but not on $\mathrm{k}_{et}^{\mathrm{eff}}$. Note that the numerical value of $\mathrm{k}_{et}^{\mathrm{eff}}$ depends on the properties of the triplet excited state of the dye while k_{ter}^{eff} depends on the chemical properties of the colliding radicals in solution and not on the photoexcited dye ${}^{\mathrm{T_1}}\mathrm{D}$ concentration.

In summary, at extremely low sample concentration and in the presence of excess dye the nuclear spin polarization is expected not to depend directly on the ${}^{T_1}D^{SS}$ concentration and on the photochemical properties of the dye. On the other hand, nuclear spin polarization is primarily governed by the characteristics of the radical states of the dye and of the molecule of interest, as these characteristics affect parameters including radical termination rate constant, g-factor, hyperfine coupling constants and $\mathrm{T}_1^{\mathrm{M}^{\bullet+}}$. These parameters, in turn, influence the value of most terms (i.e., all but T_1^M and $[M]_0$) of relation S8.

As a consequence, the weak laser-power dependence observed in Fig. 5 (see main manuscript) at 500 nM Trp concentration is ascribed to the fact that both the low-sample-concentration (i.e., $[\mathrm{M}]_\mathrm{o} < 1$ μM) and the $[{}^{\mathrm{T1}}\mathrm{D}^{\mathrm{SS}}] >> [\mathrm{M}]_o$ regimes apply to panel c of Fig. 5. Hence, relation S8 applies, and nuclear spin polarization is expected to depend only weakly (or not at all, under limiting conditions) on ${}^{T_1}D^{SS}$ concentration, which is modulated by laser power. This prediction is fully consistent with the experimentally observed weak laser-power dependence of photo-CIDNP at 500 nM Trp concentration, shown in Figure 5c.

1.2. Effect of ionic strength. According to equation 1 of this article, reproduced below, the following expression applies to signal-to-noise

$$S/N \propto U_S/U_N \propto 1/\sqrt{T_c R_c + T_a[R_c + R_s] + T_s R_s} \quad , \qquad \text{(S9)}$$

where U_S and U_N are the electrical currents induced by the signal and by the noise, respectively. In addition, T_c, T_a and T_s denote the temperatures of the coil, preamplifier and sample, respectively, and R_c and R_s are the resistance of the coil in the absence of sample and the added resistance of the coil when the sample is in the probe, respectively[4].

Hence the NMR signal-to-noise ratio (S/N) decreases as the electrical resistance due to the sample, R_S, increases. The latter parameter is related to ion concentration according to[4]

$$R_S \propto \sigma = \sum_i c_i q_i \lambda_i \quad , \qquad \text{(S10)}$$

where σ is the sample conductivity, c_i is the concentration of the i^{th} ion, and q_i and λ_i are the charge and mobility of the i^{th} ion, respectively. It follows that the NMR sample resistance increases with salt concentration, consistent with the qualitative expectation that salts give rise to charge shielding.

For cryogenic probes, the coil and preamplifier temperatures T_c and T_a, respectively, are ca. 12-25 K[5], while sample temperature T_S is typically close to room temperature. Hence the small values of T_c and T_a minimize the noise produced by cryogenic probes relative to room-temperature probes, with resulting better S/N.

The $T_\mathrm{S} R_\mathrm{S}$ term in the denominator of equation S9 is dominant for cryogenic probes. Given that the resistance of the sample R_S increases at high ionic strength, high salt concentration is expected to disfavor S/N in cryogenic probes via an increase in noise level. In addition, high ionic strength is also known to decrease the quality of the NMR signal (as opposed to the noise) due to less efficient probe tuning and increased pulse lengths[5].

In short, both NMR signal and noise levels are more unfavorable at high salt concentration, and this effect is particularly pronounced for cryogenic probes due to the dominance of the $T_S R_S$ term.

High ionic strength is often required in biomolecular NMR experiments, e.g., in experiments involving nucleic acids and samples under physiologically relevant conditions. Hence, we decided to assess the effect of high salt concentration on photo-CIDNP data collected on spectrometers equipped with a cryogenic probe. We performed photo-CIDNP experiments on 1 mM Trp and 2.5 μM fluorescein in the presence of the GO and CAT oxygen-scavenging enzymes under both dark (laser-off) and light (laser-on) conditions. A high concentration of sample was used to enable detection of significantly reduced signal at high salt concentration.

As shown in Supplementary Figure 3a, as expected, we observed an increase in the noise level up to ca. 2-fold at high NaCl concentration (i.e., 300 – 500 mM [NaCl]), under dark (i.e., laser off) conditions. In parallel, not surprisingly we also detected a significant decrease in signal (Supplementary Fig. 3b). This decrease, however, was more pronounced under light than dark conditions, suggesting that the photo-CIDNP enhancement is ionic-strength-dependent in the presence of a cryogenic probe.

This result is not entirely unexpected, considering that it is known[6, 7] that photo-CIDNP intensities are significantly influenced by Coulombic forces between radical ion pair components, given that translational diffusion of ions is generally influenced by the presence of other ions in solution. More specifically, two key processes affecting the photo-CIDNP radical ion pair, triplet-singlet mixing and back electron transfer, require the radical pair to first separate and then rejoin through diffusive motions[2].

The attractive Columbic interaction between two ionic radicals of opposite sign, including the photo-CIDNP radical ion pair, greatly enhances the likelihood that the two elements of a radical pair rejoin. On the other hand, other ions in solution shield this interaction and are therefore expected to decrease photo-CIDNP polarization enhancement.

Next we will provide a more rigorous treatment aimed at quantifying the effect of ionic strength on photo-CIDNP enhancements in the presence of a cryogenic probe.

The potential energy $U(r)$ resulting from the Columbic interaction between two ions in solution can be estimated via the Debye-Hückel relation[8]

$$U(r) = \frac{z_1 z_2 e^2}{4\pi\varepsilon_0 \varepsilon_r r(1+\kappa a)} \exp\left(-\kappa\left(r-a\right)\right) \quad , \tag{S11}$$

in the SI system, where z_1, z_2 is the charge of the 1st and 2nd ion (e.g., as in a photo-CIDNP radical pair), e is the charge of the electron , ε_0 is the vacuum permittivity, ε_r is the relative permittivity, r is the distance between the two ions, and a is the contact distance between the ions. The term κ denotes the Debye screening wave vector, which is the inverse of the Debye length, and is defined as[8]

$$\kappa = \sqrt{\frac{e^2}{\varepsilon_0 \varepsilon_r k_B \mathrm{T}} \sum_j z_j^2 \rho_j} \ , \tag{S12}$$

where z_j is the charge number of the jth ion, ρ_j is number density (i.e., $\rho_j = \frac{N_j}{\mathrm{V}}$, where N_j is the number of jth ions in volume V, k_B is the Boltzmann constant, and T is the temperature).

The ionic strength is defined as

$$I = \frac{1}{2}\sum_j z_j^2 c_j = \frac{1}{2N_A}\sum_j z_j^2 \rho_j \quad , \tag{S13}$$

where c_j is the ion concentration, and N_A is Avogadro's number. From equations S11 – S13 we conclude that at higher ionic strength κ increases, leading to a less negative $U(r)$. It follows that high ionic strength weakens Columbic interactions and is therefore expected to cause a decrease in the strength of the interactions within the elements of the photo-CIDNP radical pair, causing smaller photo-CIDNP enhancements.

Let's now denote the probability of geminate recombination per triplet precursor radical pair as $F^{*}(\omega_{TS})$, where ω_{TS} denotes the triplet-singlet mixing frequency. Let's also assume, on a first-order approximation, that the elements of a singlet-radical pairs always react upon encounter, giving rise to recombination products[2]. Then F^{*} can be expressed as follows[7, 9]

$$F^{*}(\omega_{TS}) = F^{o,*}(\omega_{TS})\, f^{*} \quad , \tag{S14}$$

where $F^{o,*}(\omega_{TS})$ corresponds to $F^{*}(\omega_{TS})$ for radical pair diffusion as a pure random walk (i.e., in the absence of any Coulombic potential), and f^{*} is the correction factor that takes Coulombic attraction into account.

Pedersen and Freed showed that the correction factor f^{*} can be represented as[7, 9]

$$f^{*} = \frac{1}{a\int_{a}^{\infty} \exp\left(\frac{U(r)}{k_{\mathrm{B}}\mathrm{T}}\right)\frac{dr}{r^{2}}} \quad , \tag{S15}$$

where, as previously noted, *a* is the contact distance between the ions

Let's now recast relation S14 into a more directly useful, simplified form. First, we define the triplet-single mixing frequency of a radical pair $\omega_{TS,\chi}$ as[6]

$$\omega_{TS,\chi} = \frac{1}{2}\left[(g_{\mathrm{M}} - g_{\mathrm{D}})\mu_{\mathrm{B}}\hbar^{-1}\,\mathrm{B_o} + \left(\sum_{i} A_{\mathrm{M,i}} M_{\mathrm{M,i}} - \sum_{j} A_{\mathrm{D,j}} M_{\mathrm{D,j}}\right)\right] \tag{S16}$$

where the subscript χ denotes a specific nuclear-spin configuration of the dye and molecule of interest, g_{M} and g_{D} are the g factors for the molecule of interest and the dye, respectively, μ_{B} is Bohr's magneton, $\hbar$ is Planck's constant $\mathrm{B_o}$ is an external magnetic field, $A_{\mathrm{M,i}}$ and $A_{\mathrm{D,j}}$ are hyperfine coupling constants of *i*th and *j*th nucleus of the molecule of interest and the dye, respectively, and $\mathrm{M_{M,i}}$ and $\mathrm{M_{D,j}}$ are the z-components of the nuclear spin angular momentum quantum number (i.e., +1/2 and –1/2 for the α and β nuclear spins) of the molecule of interest and the dye, respectively.

It can be shown that, for $\frac{\omega_{TS,\chi}a^2}{D} << 1$ one can approximate $F^{o,*}\left(\omega_{TS}\right)$ for any given nuclear configuration[6, 7] to

$$F^{o,*}\left(\omega_{TS,\chi}\right) \approx \sqrt{\frac{\omega_{TS}a^2}{4D}} \quad . \qquad \text{(S17)}$$

Now let's define the effective contact distance *a** as the maximum distance corresponding to a 100 % probability of collision between the two radical-pair components.

$$a^* = a\, f^* \quad . \qquad \text{(S18)}$$

For a specific nuclear-spin configuration, equations S17 can be replaced into S14, and S18 can then be substituted in the resulting expression, so that relation S14 can be recast as

$$F^*\left(\omega_{TS,\chi}\right) = af^*\sqrt{\frac{\omega_{TS,\chi}}{4D}} = a^*\sqrt{\frac{\omega_{TS,\chi}}{4D}} \quad . \qquad \text{(S19)}$$

The physical interpretation of eq. S19 is that high ionic strength, which renders Coulombic interactions between two ions of opposite charge shorter-range, decreases the effective contact distance of the radical pair *a**, thereby decreasing $F^*\left(\omega_{TS,\chi}\right)$. Hence the probability of geminate recombination of the triplet radical pair in a given nuclear configuration decreases at high ionic strength.

The consequences of relation S19 for photo-CIDNP can be more explicitly appreciated upon considering the proportionality

$$\xi^{\mathrm{G,k}}\Phi_{\mathrm{G}} \propto \sum_{m\in N_{k\alpha}} F^*\left(\omega_{TS,i}\right) - \sum_{n\in N_{k\beta}} F^*\left(\omega_{TS,j}\right) = a^*\left(\sqrt{\frac{\omega_{TS,m}}{4D}} - \sqrt{\frac{\omega_{TS,n}}{4D}}\right), \qquad \text{(S20)}$$

where the summations apply to specific nuclear configurations *m* and *n*, defined so that nucleus k is in the α and β nuclear spin states in configurations *m* and *n*, respectively. Equation S20 shows that photo-CIDNP polarization, which is proportional to $\xi^{\mathrm{G,k}}\Phi_{\mathrm{G}}$ (see eq. S1), decreases at high ionic strength.

Relation S14, hence also relation S20, are only valid for short-range interactions. Hence they hold only at relatively high ionic strength (typically $\kappa a \le \frac{1}{4}$)[6]. A more accurate description of the effect of ionic strength on photo-CIDNP requires the use of a more elaborate correction factor that takes the dependence on the triple-singlet transition frequency $\omega_{TS,\chi}$ into account[6]. However, this detailed treatment is beyond the scope of our study. At this juncture, we merely aim at showing that photo-CIDNP enhancement is expected to decrease at high ionic strength.

Next, we took advantage of equations S1 and S20 to theoretically predict the ratio of H$^{\alpha}$ Trp photo-CIDNP enhancements in the absence and presence of high NaCl concentration (in 10 mM buffer), upon using the relation

$$\begin{aligned}&\frac{\text{light Integral of H}^{\alpha}\left(\text{[NaCl]}\right)}{\text{light Integral of H}^{\alpha}\left(\text{[NaCl]=0}\right)}\frac{\text{dark Integral of H}^{\alpha}\left(\text{[NaCl]=0}\right)}{\text{dark Integral of H}^{\alpha}\left(\text{[NaCl]}\right)}\\&=\frac{\tilde{P}_k^{\text{M,SS}}\left(\text{[NaCl]}\right)}{\tilde{P}_k^{\text{M,SS}}\left(\text{[NaCl]}\right)}\approx\frac{\xi^{\text{G}}\Phi_{\text{G}}\left(\text{[NaCl]}\right)}{\xi^{\text{G}}\Phi_{\text{G}}\left(\text{[NaCl]=0}\right)}\approx\frac{f^{*}\left(\text{[NaCl]}\right)}{f^{*}\left(\text{[NaCl]=0}\right)}\end{aligned}, \qquad \text{(S21)}$$

where the factor $\frac{\text{dark Integral of }^{\alpha}\text{H}\left(\text{[NaCl]=0}\right)}{\text{dark Integral of }^{\alpha}\text{H}\left(\text{[NaCl]}\right)}$ takes into account the photo-CIDNP-independent detrimental effect of high ionic strength on probe performance. In the theoretical predictions, we assumed constant and equal concentrations of all non-NaCl species. This assumption is reasonable as the theoretical predictions resulting from equation S21 were aimed at matching our experimental data collected at a relatively high Trp and dye (fluorescein) concentration, as shown in Supplementary Figure 3c. Experimental dilution effects resulting from addition of salts were small. Hence only kinetic processes that involve net charges, i.e., radical ion pair recombination, are expected to be influenced by salt concentration.

Supplementary Figure 3c shows a comparison between the theoretical (predicted via eq. S21) and experimental photo-CIDNP polarization data on the Trp H$^{\alpha}$ resonance. Theory and experiments are in excellent agreement. We conclude that Coulombic interactions play a significant role in photo-CIDNP polarization, and that at high ionic strength photo-CIDNP polarization decreases in a predictable fashion. It is worth noticing that despite the losses in enhancement at high salt concentration there are still net enhancements observed, even at high salt concentration, as shown in Supplementary Figure 3c.

1.3. Nonselective and selective longitudinal relaxation in constant-time SOFAST-HMQC (CT-SOFAST-HMQC).

In order to fully understand the most appropriate choices of NMR parameters in SOFAST HMQC experiments, especially recycle delays (see also sections 1.4 – 1.5), it is helpful to start by briefly reviewing a few fundamental aspects of nuclear spin relaxation.

Given a proton *i* in spatial proximity with other protons *j*, the longitudinal relaxation of nuclear spin *i* is described by the well-known Solomon equations[10, 11]

$$-\frac{d(i_z - i_z^0)}{dt} = \sum_j \rho_{ij}(i_z - i_z^0) + \sum_j \sigma_{ij}(j_z - j_z^0) \ , \qquad \text{(S22)}$$

where i_z and j_z denote the z-magnetization components of nuclear spins *i* and *j*, respectively, and i_z^0, j_z^0 are the corresponding equilibrium magnetizations. The ρ_{ij} and σ_{ij} parameters denote the direct and cross relaxation rate constants of spin *i* due to its dipole-dipole interaction with spin *j*, respectively. Other longitudinal relaxation mechanisms (e.g., chemical shift anisotropy) are neglected here, given the dominant role of magnetic dipole-dipole relaxation. The direct- (ρ_{ij}) and cross- (σ_{ij}) relaxation rate constants are functions of the spectral density *J(ω)*, which is a measure of the probability of local-field fluctuations at given angular frequencies ω[12], yielding

$$\rho_{ij} = \frac{\mu_0^2 \gamma_H^4 \hbar^2}{320\pi^2 r_{ij}^6}[3J(\omega_0) + 6J(2\omega_0) + J(0)] \qquad \text{(S23)}$$

$$\sigma_{ij} = \frac{\mu_0^2 \gamma_H^4 \hbar^2}{320\pi^2 r^6}\left[6J(2\omega_0) - J(0)\right] \ , \qquad \text{(S24)}$$

where μ_0 is the vacuum permeability, γ_H denotes the gyromagnetic ratio of the proton, r_{ij} is the distance between spins *i* and *j*, ω_0 is the Larmor frequency of the proton,

$$J(\omega) = \frac{2\tau_c}{1 + \omega^2 \tau_c^2} \qquad \text{(S25)}$$

is the spectra density, and τ_c is the rotational correlation time, which is proportional to the rotation tumbling time. Note that for large molecules $\omega_0\tau_c \gg 1$; therefore the *J(0)* terms dominate over the $J(\omega_0)$ and $J(2\omega_0)$ terms.

It turns out that the cross relaxation rate constant σ_{ij} obeys the relation $\sigma_{ij} > 0$ when $\omega_0\tau_c \ll \sqrt{\tfrac{5}{4}}$ (i.e., at short τ_c, small molecules), and $\sigma_{ij} < 0$ when $\omega_0\tau_c \gg \sqrt{\tfrac{5}{4}}$ (i.e., at long τ_c, large molecules). On the other hand, the direct relaxation rate constant ρ_{ij} is positive (i.e., $\rho_{ij} > 0$) for all values of τ_c, i.e., for small and large molecules.

In the case of non-selective radiofrequency pulses, all spins i and j are excited, hence $i_z^0 = j_z^0$ and $i_z = j_z$. under initial conditions (i.e., at *t* = 0), equation S22 becomes

$$-\frac{d(i_z - i_z^0)}{dt}\bigg|_{t=0}^{non-sel} = \sum_j (\rho_{ij} + \sigma_{ij})(i_z - i_z^0) \quad , \qquad \text{(S26)}$$

thus the initial relaxation rate constant $R_{init}^{non-sel}$ can be expressed as

$$R_{init}^{non-sel} = \sum_j (\rho_{ij} + \sigma_{ij}) \quad . \qquad \text{(S27)}$$

Conversely, in the case of selective excitation of spin *i*, the j spins are not perturbed, thus $j_z = j_z^0$ at *t* = 0, and relation S22 becomes

$$-\frac{d(i_z - i_z^0)}{dt}\bigg|_{t=0}^{sel} = \sum_j \rho_{ij}(i_z - i_z^0) \qquad \text{(S28)}$$

Under these conditions, the initial selective longitudinal relaxation rate constant R_{init}^{sel} can be expressed as

$$R_{init}^{sel} = \sum_j \rho_{ij} \quad . \qquad \text{(S29)}$$

Upon replacing relations S23 and S24 into relation S27, one immediately notices that the *J(0)* spectral density terms cancel out in the case of non-selective longitudinal relaxation, preventing the *J(0)*-mediated relaxation path. Conversely, the absence of the cross-relaxation term upon selective resonance excitation (see eqn. S29) prevents the *J(0)* term cancellation, and renders the initial selective relaxation faster than the initial non-selective relaxation in the case of macromolecules, where the $J(0)$ term is dominant (i.e., $J(0) >> J(2\omega)$). In our experiments, we regard the experimentally measured longitudinal relaxation rate constants (for data collected across several seconds) as providing approximate, representative estimates of the initial relaxation rate constants R_{init}^{sel} and $R_{init}^{non-sel}$, upon selective and non-selective excitation, respectively.

Longitudinal relaxation times (T_1) are defined as the inverse of the corresponding relaxation rate constants. Hence, taking the above arguments into account, one can deduce that selective (or semi-selective, in case a group of nuclear spins are excited) longitudinal relaxation times are shorter than the corresponding non-selective parameter for proteins. due to the absence (or partial absence) of the σ_{ij} cross-relaxation terms.

In our CT-SOFAST-HMQC experiments, the longitudinal relaxation times (T_1) of the protons of interest fall anywhere between the selective and non-selective values, depending on which and how many other protons are excited via the semi-selective π and α pulses (Supplementary Fig. 5).

The most relevant implications of the above statements are apparent in the sections below.

1.4. Parameter optimization in CT-SOFAST-HMQC. The sensitivity *(S/N)ₜ* of the ^{1}H,^{13}C CT-SOFAST-HMQC NMR pulse sequence, where sensitivity is defined as signal-to-noise-per square root of unit time (see eq. S33), is proportional to a number of NMR parameters according to[13]

$$(S/N)_t \propto \frac{(1-\exp(-T_{rec}/T_1))\sin\beta}{1-\exp(-T_{rec}/T_1)\cos\beta}\frac{1}{\sqrt{T_{scan}}} \ , \tag{S30}$$

$$\cos\beta_{opt} = \exp(-T_{rec}/T_1) \ , \tag{S31}$$

where T_{rec} is the effective relaxation delay of the pulse sequence, corresponding to the time from the 180^0 ^{1}H selective pulse to the following α pulse (Supplementary Fig. 5a). T_1 is the longitudinal relaxation time constant experienced by the ^{1}H of interest, T_{scan} is the duration of one full scan, $\beta = \pi - \alpha$ is the effective excitation flip angle, and β_{opt} is the optimal β value for any given T_{rec}, also known as the Ernst angle[14].

To optimize the flip angle α and the T_{rec} delay, we measured the selective T_1 (see section 1.3) of different resonances (Supplementary Table 1 and Methods section), and used the results to estimate optimal α and T_{rec} values according to equations S30 and S31 by numerical optimization. Finally, further fine-tuning of the latter two parameters was carried out empirically at the spectrometer (see Supplementary Table 2).

The importance of selective and nonselective longitudinal relaxation in SOFAST-HMQC, which is related to proper choices of α and T_{rec}, is briefly highlighted in the next section.

1.5. Importance of longitudinal relaxation in CT-SOFAST-HMQC. One well-known reason for employing a semi-selective pulse in SOFAST HMQC-type experiments[13] is to excite only amide protons in ^{1}H,^{15}N SOFAST-HMQC of proteins so that the non-perturbed protons are enabled to interact with the excited protons, which then undergo faster longitudinal relaxation. In this way, the T_1 values of the excited protons decrease and faster signal averaging can be carried out[15]. Consistent with this idea and according to the arguments outlined in the previous section, semi-selective excitation, leading to transitions of all the amide protons (but not any other protons), triggers dipole-dipole relaxation with features that are intermediate between those described by equation S27 and equation S29. As a result, the sensitivity of the experiment increases, given the faster signal averaging enabled by the shorter relaxation delay that can be employed thanks to the more efficient longitudinal relaxation.

In this work, we focus on an analogous experiment targeting proton and carbon resonances in constant-time mode, ^{1}H-^{13}C CT-SOFAST-HMQC. A brief justification for the role played by longitudinal relaxation in the version of this experiment targeting aromatic and alpha H-C pairs is provided in sections 1.6 and 1.7, respectively.

1.6. Detection of H-C aromatic pairs via ^{1}H,^{13}C CT-SOFAST-HMQC: role of longitudinal relaxation. In our ^{1}H,^{13}C CT-SOFAST-HMQC experiments on aromatic protons according to the pulse sequences in Supplementary Figure 5a, we found that the optimal recycle delay t_r is relatively long (~0.5 s) compared to the ~0.1-0.2 s of typical ^{1}H,^{15}N SOFAST-HMQC experiments. This observation suggests that the effective longitudinal relaxation rate is not reduced despite the use of proton semi-selective pulses to excite the aromatic region.

To verify this hypothesis, we designed the pulse sequence in Supplementary Figure 6 and used it to experimentally determine the longitudinal relaxation rates of the aromatic protons. This pulse sequence is inversion-recovery-based except that soft 180^0 ^{1}H shaped pulses are employed to selectively invert aromatic protons, followed by standard ^{1}H,^{13}C CT-SOFAST-HMQC pulses for detection.

We used this pulse sequence to determine semi-selective T_1 values of the aromatic protons of both Trp and the SH3 protein. We then compared the results with standard non-selective T_1 measurements carried out with the ^{1}H inversion-recovery pulse sequence, with presaturation for solvent suppression. The results are shown in Supplementary Table 1.

Inspection of Supplementary Table 1 shows that the semi-selective and non-selective longitudinal relaxation times of aromatic protons are similar. This observation applies to both free Trp and to the SH3 protein. Hence, applying semi-selective pulses to the aromatic protons of free Trp does not have a significant impact on longitudinal relaxation. This observation justifies our choice of relatively long recycle delays in the ^{1}H,^{13}C CT-SOFAST-HMQC pulse sequence.

The similarity between the non-selective and semi-selective longitudinal relaxation values of Trp is not surprising and can be rationalized upon considering the small molecular size of Trp, leading to fast-tumbling rates so that $\omega_0\tau_c \ll \sqrt{\frac{5}{4}}$. Upon inspection of relations S23, S24, S27 and S29, and noting that the magnitude of $J(0)$, $J(\omega_0)$ and $J(2\omega_0)$ is essentially identical within this tumbling regime, the semi-selective longitudinal relaxation time of Trp is not expected to be shorter than the corresponding non-selective value. If anything, T_1 is expected to be somewhat longer under semi-selective excitation conditions. However, this effect is not significant given that the number of non-excited protons under aromatic-only excitation conditions is rather small, for Trp.

Conversely, in the case of the SH3 protein, where $J(0) \gg J(\omega_0), J(2\omega_0)$, equations S23, S24, S27 and S29 predict an expected faster relaxation in the case of semi-selective excitation of aromatic protons.

However, given that the major source of relaxation of aromatic protons in the SH3 protein are other aromatic protons in closest spatial proximity, semi-selective excitation is not expected to significantly vary the relaxation features, fully consistent with our experimental observations.

1.7. Detection of H^{α}-C^{α} pairs via $^{1}H,^{13}C$ CT-SOFAST-HMQC: role of longitudinal relaxation.

Similar arguments to those outlined in the previous section apply to the interpretation of semi-selective and non-selective T_1 measurements of H^{α} protons reported in Supplementary Table 1. In the case of H^{α} protons of the SH3 protein, however, experimentally observed T_1 values of H^{α} protons are ca. 3-fold shorter upon semi-selective excitation. This result is ascribed to the fact that the H^{α} protons are in close spatial proximity to the H^{β}, H^{N} and some of the Trp aromatic protons. Conveniently, these protons have significantly different chemical shift from the H^{α} protons, hence semi-selective excitation of H^{α} protons is effective at factoring out both H^{β}, H^{N} and aromatic protons.

In the case of the Trp, given its high tumbling rates (see arguments above), less efficient relaxation is predicted (hence longer T1) upon semi-selective excitation. This expectation is consistent with the experimentally observed slight increase in longitudinal relaxation time, as shown in Supplementary Table 1. Hence the detection of $H^{\square}$ protons of small molecules like Trp does not provide faster longitudinal relaxation benefits upon semi-selective excitation. Shorter relaxation delays and faster signal averaging cannot be applied, and ^{1}H,^{13}C-SOFASTHMQC is not a particularly convenient pulse sequence, in this case.

In the case of macromolecules like the SH3 protein, however, the zero-frequency spectral density term dominates in equations S23 and S24, and one expects longitudinal relaxation times of H^{α} protons to be shorter, upon semi-selective excitation. This prediction is indeed consistent with the experimental findings of Supplementary Table 1, and in this case the ^{1}H,^{13}C-SOFAST HMQC pulse sequence is expected to provide benefits due to the opportunity of fast data collection.

On the other hand, a practical challenge inherent in the SOFAST HMQC experiment prevented us from being able to collect reliable ^{1}H,^{13}C-CT-SOFAST HMQC reference data on the H^{α} protons of both

Trp and the SH3 protein in aqueous solution. When we attempted to collect ^{1}H,^{13}C-CT-SOFAST-HMQC data on the Trp H^{α} protons with the pulse sequence of Supplementary Figure 5b, which includes a selective pulse centered at 4.5 ppm and solvent presaturation during the relaxation delay, we experienced signal losses ranging from 50% to > 90% compared to ^{1}H-^{13}C-CT-SE-HSQC. These losses may be due to the fact that the solvent pre-saturation pulse partially saturates the H^{α} polarization. Other common solvent suppression schemes, e.g., WATERGATE (including 3919[16, 17], W5[18] and others), are not compatible with ^{1}H,^{13}C-CT-SOFAST-HMQC because they perturb all protons, thus the protons of interest relax by non-selective T_1 mechanisms, rather than by selective T_1.

Given the above, a proper implementation of ^{1}H,^{13}C-CT-SOFAST-HMQC on H^{α} protons requires the absence of solvent suppression schemes. This is only possible upon data collection in 100% D_2O rather than in 95% water. Data acquisition in deuterated solvent is a significant limitation and is often not desirable. In addition, all of the data shown in this work is in mostly protonated aqueous solvent ($D_2O \leq$ 10 %). Hence, for consistency, we did not include any reference $H^{\square}$ experiments in fully deuterated solvent.

In summary, due to the above features of ^{1}H,^{13}C-SOFAST-HMQC for $H^{\square}$ protons, we were not able to provide experimental $H^{\square}$ data for this pulse sequence in protonated solvent for either Trp or the SH3 protein, in this study.

2. Supplementary Methods

2.1. Signal-to-noise ratio (S/N). The S/N was evaluated via the relation below[14]

$$\left(\frac{S}{N}\right)=\frac{S}{2\sigma_N}\cong\frac{2.5\times S}{\left\langle N_{ptp}\right\rangle}\quad, \qquad \text{(S32)}$$

where S is the experimentally measured signal amplitude, σ_N is the r.m.s. noise amplitude, and $\langle N_{ptp}\rangle$ is the experimentally determined peak-to-peak noise amplitude within 100 zero crossings, with $\langle N_{ptp}\rangle \cong 5.0\,\sigma_N$.

2.2. NMR sensitivity. NMR sensitivity is denoted as $(S/N)_t$ and is defined as[19]

$$\left(\frac{\mathrm{S}}{\mathrm{N}}\right)_{\mathrm{t}} = \frac{S/N}{\sqrt{t}} \cong \frac{2.5\times \mathrm{S}}{\left\langle \mathrm{N_{ptp}} \right\rangle \sqrt{\mathrm{t}}} \quad , \qquad \text{(S33)}$$

where t is the total NMR experiment time.

The NMR sensitivity enhancement ε_{pC} is defined as

$$\varepsilon_{pC} = \frac{\mathrm{I_{light}} / [\mathrm{M}]_{\mathrm{light}}}{\mathrm{I_{dark}} / [\mathrm{M}]_{\mathrm{dark}}} \quad , \qquad \text{(S34)}$$

where I_{dark} and I_{light} denote the integrated areas of the resonance of interest under dark and light conditions, respectively. The $[M]_{dark}$ and $[M]_{light}$ parameters denote the concentration of the molecule of interest under dark and light conditions, respectively. Importantly, equation S34 requires the dark and light data to be acquired with identical acquisition and processing parameters, including an identical number of scans. In addition, sample concentrations and number of scans under dark and light conditions need to be adjusted so that a signal of measurable intensity is detected.

2.3. Photo-CIDNP polarization. The % nuclear-spin polarization under light (i.e., laser on) conditions is denoted as, $P_{\%}$, and was experimentally determined via relation

$$P_{\%} = \frac{\mathrm{I_{light}} / [\mathrm{M}]_{\mathrm{light}}}{\mathrm{I_{dark}} / [\mathrm{M}]_{\mathrm{dark}}} * P_{\%,\mathrm{therm}} = \varepsilon_{pC} * P_{\%,\mathrm{therm}} \quad , \qquad \text{(S35)}$$

where $P_{\%,\mathrm{therm}}$ denotes the nuclear-spin polarization at thermal equilibrium. The latter parameter was estimated to be 0.0012%, via relation

$$P_{\%,\mathrm{therm}} = \frac{\exp\left(-\frac{\gamma B_0 \hbar}{2k_B T}\right) - \exp\left(\frac{\gamma B_0 \hbar}{2k_B T}\right)}{\exp\left(-\frac{\gamma B_0 \hbar}{2k_B T}\right) + \exp\left(\frac{\gamma B_0 \hbar}{2k_B T}\right)} \approx \frac{\gamma B_0 \hbar}{2k_B T} \quad , \qquad \text{(S36)}$$

where γ is the ^{13}C gyromagnetic ratio, B_0 is the applied magnetic field, k_B is Boltzmann constant and T is the sample temperature.

2.4. Reference NMR experiments. Three classes of reference NMR experiments were run, namely laser-off (dark) ^{13}C PREPRINT, ^{1}H-^{13}C sensitivity-enhanced HSQC with constant time evolution (^{1}H-^{13}C CT-SE-HSQC[20]) and ^{1}H,^{13}C SOFAST-HMQC with constant time evolution (^{1}H,^{13}C CT-SOFAST-

HMQC[13]). These experiments served as comparisons for laser-on (light) ^{13}C PREPRINT. All ^{13}C PREPRINT data were collected at 600 MHz. The ^{1}H,^{13}C CT-SE-HSQC and ^{1}H,^{13}C CT-SOFAST-HMQC data were collected on a 900 MHz (21.2 T) Bruker Avance III HD NMR spectrometer equipped with a ^{1}H {^{13}C,^{15}N} TCI-F cryogenic probe, unless otherwise noted. The last two experiments represent the highest-sensitivity non-laser-assisted comparisons, and were run at the highest locally available magnetic field to maximize the achievable S/N. No fluorescein, GO, CAT or D-glucose were added to the samples employed in these reference experiments.

The pulse sequence used for ^{1}H,^{13}C CT-SOFAST-HMQC is shown in Supplementary Figure 5a. This experiment was only run for aromatic resonances, and flip angle α and relaxation delay t_r were optimized given the semi-selective T_1 for aromatic resonances, which was independently determined (see Supplementary Table 1). All ^{1}H,^{13}C CT-SOFAST-HMQC experiments were performed using a sweepwidth of 10 kHz, 1,024 total points and a 0.48 s relaxation delay.

2.5. Preparation of bacterial cell-free NMR sample. A bacterial cell-free transcription-translation mixture was assembled starting from an S30 extract (A19 *E.coli* cell strain) prepared according to published protocols[21]. The cell-free transcription-translation mixture (100 μL) included a pET-17b plasmid (50 μg/ml) encoding the wild-type sperm whale apoMb gene and other components as described[21], with the following exceptions. The concentration of all the amino acids was 1 mM. The following labeled amino acids were used: ^{15}N-^{13}C-Trp, ^{15}N-Ala, ^{15}N-Glu, ^{15}N-Leu, ^{15}N-Lys, ^{15}N-Val (Cambridge Isotope Laboratories, Tewksbury, MA), with the remaining amino acids being unlabeled. A 30 kDa molecular weight cutoff Pierce 96-well dialysis strip (Thermo Scientific, Rockford, IL) was used against 8 mL of dialysis buffer including all the amino acids[21] at 1mM concentration. Dialysis was carried out overnight upon gentle shaking at 37 °C. We prepared a cell-free mixture lacking T7 RNA polymerase, so that no transcription-translation could take place in the sample. This procedure enabled NMR analysis of labeled Trp in the bacterial cell-free environment in the absence of any consumption via incorporation into proteins. Some of the Trp may have been incorporated into its cognate tRNA and(or) could have undergone some other metabolic processes within the cell-free-system environment.

On the other hand, the spectra in Figure 6 show no evidence for any Trp-metabolism byproducts, so this was not a concern for the purpose of the qualitative analysis displayed in this Figure.

Following the overnight dialysis step, the sample volume increased to ca. 140 μl. The photo-CIDNP-related components (0.20 μM GO, 0.20 μM CAT, 2.5 μM fluorescein, 10 % D_2O with 2.5 mM glucose added last) were added so that the final cell-free mixture contained 2.84 mM tris acetate, 0.72 mM magnesium acetate, 1.80 mM ammonium acetate, 3.60 mM potassium acetate, 0.08 mM calcium acetate, 0.50 mM KCl and 16.57 mM potassium phosphate. Samples were incubated for ca. 20 min before photo-CIDNP data collection. The total ionic strength was ca. 65 mM. The final concentration of Trp was 25 μM.

2.6. Cell-free NMR data collection and analysis. 1D ^{13}C PREPRINT photo-CIDNP NMR data on the cell-free-system sample were collected at 24 °C with the same acquisition parameters used for the data in Figures 2 and 3 (see Methods section of main article) except that the 488 nm laser-pulse duration was set to 0.05s. Data processing was carried out with the MestReNova (v. 12.0, Mestrelab Research, SL, Santiago de Compostela, Spain). ^{1}H chemical shift referencing was done with external 4,4-dimethyl-4-silapentane-1-sulfonic acid (DSS). Data were processed by zero-filling to 4096 complex points, using an exponential window function with 8 Hz line-broadening.

2.7. Transient absorption experiments. Transient absorption experiments were carried out at room temperature with an LP 980 transient absorption spectrometer (Edinburg Instruments, Livingston, U.K.) equipped with a tunable Opolette HE 355LD ns pulsed laser (YAG-pumped OPO, Opotek Inc., Carlsbad, CA). Each transient was collected after excitation with a single laser pulse at 488 nm (5mJ, 7 ns duration), and transient triplet-triplet absorption was detected at 650 nm. Each data set in Figure 1c reports the average readings for 200 scans. Experiments were carried out either in a quartz cuvette (1 cm pathlength) or directly in a shortened NMR tube (ca. 10 cm height, 5 mm diameter, ca. 0.5 cm pathlength) by firmly securing it to the center of a 1 x 1 cm quartz cuvette with the interfacial volume between cuvette and NMR tube filled with water. Data were reported as intensity = $\Delta OD = OD_{\text{laser on}}$ –

$OD_{\text{laser off}}$, and were fit to a single-exponential decay. Traces shown in Figure 1c were normalized so that at t=0 the exponential fit has intensity = 1 for all three data sets.

3. Appendix

Derivation of Equation S7. Let's consider the photo-CIDNP kinetic scheme of Supplementary Figure 7 at very low sample concentration, i.e. $[\mathrm{M}]_o < 1$ μM where the dye is in large excess relative to the sample, i.e. $[{}^{T1}\mathrm{D}^{SS}] >> [\mathrm{M}]_o$ (See Supplementary Results pages 3-4). The kinetic steps corresponding to the formation and depletion of $\mathrm{M}^{\bullet+}$ and $\mathrm{D}^{\bullet-}$ are rate-limited by the bimolecular steps involving the k_{et} and k_{ter} rate constants. These steps are much slower (ms timescale, given 10^9 $\mathrm{M}^{-1}\mathrm{s}^{-1}$ diffusion-controlled rate constants and μM reactant concentration) than the unimolecular triplet-singlet mixing and escape steps, which usually proceed on the μs timescale[3]. In addition, let's assume that the geminate radical pair recombines rapidly (on the μs timescale) after its formation[9] and that the probability of geminate recombination is small[9]. Under these conditions, geminate recombination has a negligible effect on the overall kinetics. Hence, one has that $k_{\mathrm{et}}^{eff} \simeq k_{\mathrm{et}}$ and $k_{\mathrm{ter}}^{eff} \simeq k_{\mathrm{ter}}$.

Given all the above assumptions, the rate laws for the time-dependent concentration of the dye and M radicals are consistent with the literature[1], and can be expressed as

$$\begin{aligned}\frac{\mathrm{d}[\mathrm{M}^{\bullet+}(t)]}{\mathrm{dt}} = \frac{\mathrm{d}[\mathrm{D}^{\bullet-}(t)]}{\mathrm{dt}} &= k_{\mathrm{et}}^{eff}[\mathrm{M}(t)][{}^{\mathrm{T}_1}\mathrm{D}(t)] - k_{\mathrm{ter}}^{eff}[\mathrm{M}^{\bullet+}(t)][\mathrm{D}^{\bullet-}(t)] \\ &\quad - k_{\mathrm{de}}[\mathrm{M}(t)][\mathrm{M}^{\bullet+}(t)] + k_{\mathrm{de}}[\mathrm{M}(t)][\mathrm{M}^{\bullet+}(t)] \\ &= k_{\mathrm{et}}^{eff}[\mathrm{M}(t)][{}^{\mathrm{T}_1}\mathrm{D}(t)] - k_{\mathrm{ter}}^{eff}[\mathrm{M}^{\bullet+}(t)][\mathrm{D}^{\bullet-}(t)]\ , \qquad \text{(S37)}\end{aligned}$$

$$[\mathrm{M}]_o = [\mathrm{M}(t)] + [\mathrm{M}^{\bullet+}(t)]\ . \qquad \text{(S38)}$$

Taking into account that $[\mathrm{M}^{\bullet+}(t)] = [\mathrm{D}^{\bullet-}(t)]$ and that, under steady-state conditions, the relation below applies

$$k_{\mathrm{et}}^{eff}[\mathrm{M}^{\mathrm{SS}}][{}^{\mathrm{T}_1}\mathrm{D}^{\mathrm{SS}}] - k_{\mathrm{ter}}^{eff}[\mathrm{M}^{\bullet+}]^2 = 0\ , \qquad \text{(S39)}$$

where the SS superscript refers to steady-state conditions. Under steady-state conditions the mass conservation equation S38 can be recast as

$$[\mathrm{M^{SS}}]=[\mathrm{M}]_{\mathrm{o}}-[\mathrm{M}^{\bullet+}] \quad . \tag{S40}$$

Substitution of equation S40 into relation S39 leads to

$$k_{\mathrm{et}}^{eff}\left([\mathrm{M}]_{\mathrm{o}}-[\mathrm{M}^{\bullet+}]\right)[{}^{\mathrm{T1}}\mathrm{D^{SS}}]-k_{\mathrm{ter}}^{eff}[\mathrm{M}^{\bullet+}]^{2}=0 \quad . \tag{S41}$$

Solution of quadratic equation S41 leads to the following expression for $[\mathrm{M}^{\bullet+}]$

$$[\mathrm{M}^{\bullet+}]=\frac{-\left(k_{et}^{eff}/k_{\mathrm{ter}}^{eff}\right)[{}^{\mathrm{T1}}\mathrm{D^{SS}}]+\left(k_{et}^{eff}/k_{\mathrm{ter}}^{eff}\right)[{}^{\mathrm{T1}}\mathrm{D^{SS}}]\sqrt{1+4\frac{[\mathrm{M}]_{\mathrm{o}}}{\left(k_{et}^{eff}/k_{\mathrm{ter}}^{eff}\right)[{}^{\mathrm{T1}}\mathrm{D^{SS}}]}}}{2} \quad . \tag{S42}$$

Under the $k_{et}^{eff}[{}^{\mathrm{T1}}\mathrm{D^{SS}}]\gg k_{\mathrm{ter}}^{eff}[\mathrm{M}]_{\mathrm{o}}$ limiting conditions, square-root term of relation S42 can be approximated according to the Taylor expansion as

$$\sqrt{1+4\frac{[\mathrm{M}]_{\mathrm{o}}}{\left(k_{et}^{eff}/k_{ter}\right)[{}^{\mathrm{T1}}\mathrm{D^{SS}}]}}\cong\left(1+\frac{1}{2}\left(4\frac{[\mathrm{M}]_{\mathrm{o}}}{\left(k_{et}^{eff}/k_{ter}\right)[{}^{\mathrm{T1}}\mathrm{D^{SS}}]}\right)-\frac{1}{8}\left(4\frac{[\mathrm{M}]_{\mathrm{o}}}{\left(k_{et}^{eff}/k_{ter}\right)[{}^{\mathrm{T1}}\mathrm{D^{SS}}]}\right)^{2}\right). \tag{S43}$$

Thus

$$[\mathrm{M}^{\bullet+}]\cong[\mathrm{M}]_{o}-\left(k_{\mathrm{ter}}^{eff}/k_{et}^{eff}\right)\left([\mathrm{M}]_{o}\right)^{2}/[{}^{\mathrm{T1}}\mathrm{D^{SS}}] \quad . \tag{S44}$$

Recalling the mass conservation equation S40, the steady-state concentration of the molecule of interest becomes

$$[\mathrm{M^{SS}}]\approx\left(k_{\mathrm{ter}}^{eff}/k_{et}^{eff}\right)[\mathrm{M}]_{o}^{2}/[{}^{\mathrm{T1}}\mathrm{D^{SS}}] \quad , \tag{S45}$$

which is identical to equation S7.

4. Supplementary References

1. Okuno, Y., Cavagnero, S. Effect of heavy atoms on photochemically induced dynamic nuclear polarization in liquids. *J. Magn. Reson.*, **286**, 172-187 (2018).
2. Okuno, Y., Cavagnero, S. Photochemically Induced Dynamic Nuclear Polarization: Basic Principles and Applications. *Emagres*, **6**, 283-313 (2017).
3. Okuno, Y., Cavagnero, S. Fluorescein: A Photo-CIDNP Sensitizer Enabling Hypersensitive NMR Data Collection in Liquids at Low Micromolar Concentration. *J. Phys. Chem. B*, **120**, 715-723 (2016).
4. Kelly, A. E., Ou, H. D., Withers, R., Dotsch, V. Low-Conductivity Buffers for High-Sensitivity NMR Measurements. *J. Am. Chem. Soc.*, **124**, 12013-12019 (2002).
5. Biswas, Z., Merkley, N., Syvitski, R. T. Biomolecular sample considerations essential for optimal performance from cryogenic probes. *Metabolomics*, **10**, 607-615 (2014).
6. Freed, J. H., Pedersen, J. B. The theory of chemically induced dynamic spin polarization. *Advances in Magnetic and Optical Resonance*, **8**, 1-84 (1976).
7. Pedersen, J. B., Freed, J. H. A hydrodynamic effect on chemically-induced dynamic spin polarization. *J. Chem. Phys.*, **62**, 1790-1795 (1975).
8. Mc Quarrie, D. A. *Statistical Mechanics* (University Science Books, Sausalito, CA, 2000).
9. Pedersen, J. B. High field CIDNP - General analytic results. *J. Chem. Phys.*, **67**, 4097-4102 (1977).
10. Cavanagh, J., Fairbrother, W. J., Parmer, A. G., Rance, M., Skelton, N. J. *Protein NMR Spectroscopy: Principles And Practice*, 2 edn (Elsevier Academic Press, Burlington, MA, 2007).
11. Gaggelli, E., Valensin, G., Kushnir, T., Navon, G. Determination of absolute values of dipolar cross-relaxation rates for ligands bound to macromolecules using double-selectiveT1. *Magn. Reson. Chem.*, **30**, 461-465 (1992).
12. Keeler, J. *Understanding NMR Specctroscopy* (John Wiley, Chichester, 2005).
13. Schanda, P., Kupce, E., Brutscher, B. SOFAST-HMQC experiments for recording two-dimensional

heteronuclear correlation spectra of proteins within a few seconds. *J. Biomol. NMR*, **33**, 199-211 (2005).

14. Ernst, R. R., Bodenhausen, G., Wokaun, A. *Principles of Nuclear Magnetic Resonance in One and Two Dimensions* (Oxford University Press, Oxford, 1987).
15. Pervushin, K., Vögeli, B., Eletsky, A. Longitudinal ^{1}H Relaxation Optimization in TROSY NMR Spectroscopy. *J. Am. Chem. Soc.*, **124**, 12898-12902 (2002).
16. Sklenar, V., Piotto, M., Leppik, R., Saudek, V. Gradient-Tailored Water Suppression for ^{1}H-^{15}N HSQC Experiments Optimized to Retain Full Sensitivity. *J. Magn. Reson., Ser A*, **102**, 241-245 (1993).
17. Piotto, M., Saudek, V., Sklenář, V. Gradient-tailored excitation for single-quantum NMR spectroscopy of aqueous solutions. *J. Biomol. NMR*, **2**, 661-665 (1992).
18. Liu, M*., et al.* Improved WATERGATE Pulse Sequences for Solvent Suppression in NMR Spectroscopy. *J. Magn. Reson.*, **132**, 125-129 (1998).
19. Lee, J. H., Okuno, Y., Cavagnero, S. Sensitivity Enhancement in Solution NMR: Emerging Ideas and New Frontiers. *J. Magn. Reson.*, **241**, 18-31 (2014).
20. Kay, L., Keifer, P., Saarinen, T. Pure absorption gradient enhanced heteronuclear single quantum correlation spectroscopy with improved sensitivity. *J. Am. Chem. Soc.*, **114**, 10663-10665 (1992).
21. Bakke, C. K., Jungbauer, L. M., Cavagnero, S. In vitro expression and characterization of native apomyoglobin under low molecular crowding conditions. *Protein Expression and Purification*, **45**, 381-392 (2006).
22. Zhang, O., Kay, L. E., Olivier, J. P., Forman-Kay, J. D. Backbone ^{1}H and ^{15}N resonance assignments of the N-terminal SH3 domain of drk in folded and unfolded states using enhanced-sensitivity pulsed field gradient NMR techniques. *J. Biomol. NMR*, **4**, 845-858 (1994).
23. Kupce, E., Freeman, R. Polychromatic Selective Pulses. *J. Magn. Reson., Ser A*, **102**, 122-126 (1993).
24. Kupce, E., Boyd, J., Campbell, I. D. Short Selective Pulses for Biochemical Applications. *J. Magn.*

Reson., Ser B, **106**, 300-303 (1995).

Supplementary Tables

Supplementary Table 1. ^{1}H non-selective and semi-selective T_1 values of Trp[a,b] and the SH3 protein[a,c].

Resonance	Semi-selective T_1 (s)	Non-selective T_1 (s)
Trp $H^{\delta 1}$	0.98 ± 0.01 s	0.70 ± 0.20 s
Trp $H^{\varepsilon 3}$	0.77 ± 0.09 s	0.81 ± 0.05 s
Trp $H^{\zeta 2}$	0.86 ± 0.06 s	0.90 ± 0.02 s
Trp $H^{\zeta 3}$	0.78 ± 0.09 s	0.88 ± 0.16 s
Trp H^{α}	0.77 ± 0.02 s	0.74 ± 0.03 s
SH3 protein, aromatic protons[d]	0.53 ± 0.00 s	0.45 ± 0.04 s
SH3 protein, H^{α} (E45, native state)[e]	0.24 ± 0.01 s	0.72 ± 0.04 s

[a] Semi-selective T_1 values were determined at 24 °C with the pulse sequence in Supplementary Figure 6. Non-selective T_1 values were assessed with the inversion-recovery pulse sequence with 10 s and 125 Hz solvent pre-saturation and ^{13}C decoupling during acquisition. Uncertainties are reported as standard errors for two independent measurements. All experiments were performed with a recycle delay t_r of 10 s and a 90° α excitation pulse (see Supplementary Figure 6).

[b] The Trp amino acid was 1 mM in water and 10% D_2O. Data collection on Trp was carried out with 8 scans.

[c] The SH3 protein was 100 μM in 500 mM Tris, 50 mM $MgCl_2$ and 5 mM KCl at pH 7.0, in the presence of 10% D_2O. Data collection on SH3 was carried out with 64 scans.

[d] Due to extensive spectral overlaps of the Trp ^{1}H aromatic resonances, one well-resolved representative resonance ($\partial_{^1H} = 6.8\ ppm,$ and $\partial_{^{13}C} = 115.5\ ppm$) was selected for these measurements.

[e] This resonance was selected because it was the only well-resolved feature in the H^{α} 1D spectral region. Assignment was based on reference[22].

Supplementary Table 2. Theoretically predicted and experimentally fine-tuned optimal values of T_{rec} and β_{opt} (see eqns. S29 and S30).

Resonance	Theoretical T_{rec} (s)	Theoretical β_{opt} (°)	Exptl. T_{rec} (s)	Exptl. β_{opt} (°)
Trp δ1[b]	0.39	47.5	0.53	60
Trp H^{α}	0.33	44.3	0.53	60

Supplementary Figure Legends

Supplementary Figure 1. Reference ^{1}H-^{13}C CT-SE-HSQC spectra of SH3 (100 µM) highlighting the ^{1}H aromatic and H$^{\alpha}$ regions of this protein. **a**, Data in the ^{1}H aromatic region were collected with 16 scans per row, and 64 complex points in the ^{13}C dimension. No assignments are available to date. **b**, Data in the H$^{\alpha}$ region were collected with 8 scans per row and 128 complex points in the ^{13}C dimension. Resonances assignments are based on published values[22].

Supplementary Figure 2. Assessment of the effect of long-term signal averaging in ^{1}H-^{13}C heteronuclear-correlation photo-CIDNP. **a**, 1D ^{13}C PREPRINT data on Trp (10 µM, aromatic ^{1}H region) collected back-to-back on the same sample. Each spectrum comprises 8 scans. **b**, Plot of cumulative S/N of the panel a data as a function of the total number of scans. **c**, Reference 1D ^{1}H-^{13}C SE-HSQC spectra acquired immediately before and after the photo-CIDNP experiment in panel a. Each experiment included 4,900 transients.

Supplementary Figure 3. Effect of salt concentration on photo-CIDNP data collected on a spectrometer equipped with a cryogenic probe. **a**, Effect of salt concentration on the peak-to-peak noise level of Trp (1 mM) in a 1D ^{13}C PREPRINT experiment performed under dark (i.e., laser-off) conditions. **b**, Comparison of the effect of salt concentration on the S/N of 1D ^{13}C PREPRINT experiments performed on 1 mM and 1 µM Trp under dark (i.e., laser-off) and light (i.e., laser-on) conditions, respectively. **c**, Comparison between theoretically estimated (via eqn. S21) and experimentally determined normalized nuclear spin polarization. Exponential apodization (with 5 Hz line-broadening) and multi-point baseline correction was applied to all the experimental data in this figure.

Supplementary Figure 4. **Overview of advantages of LC-photo-CIDNP in the presence of a cryogenic probe.** To summarize the benefits of ^{1}H-detected ^{13}C photo-CIDNP of low-concentration samples (LC-photo-CIDNP), three ^{1}H-^{13}C heteronuclear correlation spectra on 1 μM ^{13}C,^{15}N-Trp (in 90% H_20 and 10% D_2O) are shown. All spectra illustrate 1D versions of 2D LC-photo-CIDNP experiments, with the ^{13}C chemical-shift-evolution incremental delay set to zero (8 scans, other parameters as in Methods). Data were collected on a 600 MHz NMR spectrometer with identical acquisition and processing parameters except otherwise stated, under either dark (i.e., laser-off, ^{13}C PREPRINT, cryogenic probe, left image), light (i.e., laser-on, ^{13}C PRINT, room-temperature probe, central image), or light (i.e., laser-on, ^{13}C PREPRINT, cryogenic probe, right image) conditions.

Supplementary Figure 5. ^{1}H,^{13}C CT-SOFAST-HMQC pulse sequences. a, pulse program employed in experiments targeting the ^{1}H-^{13}C aromatic region. The first soft pulse had a PC-9 excitation profile[23] with flip angle α, while the second soft pulse employed an R-snob refocusing shape (180° flip angle)[24]. **b**, pulse program used in experiments targeting the H^{α}-C^{α} region. The two ^{13}C 180° selective pulses employed the Q3-surbop pulse shape (270 μs, ~16.8 kHz corresponding to a ca. 112 ppm excitation bandwidth). In all experiments, we set $\tau = 1/(4J_{CH}) = 1.7$ ms. In addition, the constant time $T=1/J_{CC}$ was set to 13.3 and 26.6 ms for data collected in the aromatic and H^{α} region, respectively. The following phase cycling was applied to both pulse sequences: φ_1=x x x x -x -x -x -x, φ_2=x -x, φ_3= -x -x y y, φ_4=y y -x -x, φ_{rec}=-x x -x x x -x x -x.

Supplementary Figure 6. **^{1}H,^{13}C CT-SOFAST-HMQC-like pulse sequences employed to determine ^{1}H T_1 values. a**, Pulse sequence used to measure ^{1}H longitudinal relaxation times in the aromatic region. This sequence is a modified version of ^{1}H,^{13}C CT-SOFAST-HMQC of Supplementary Fig. 5a. The variable delay is denoted as t_{var}. The recycle delay t_r was 10 s and the flip angle α was set to 90° to maximize signal. **b**, Pulse sequence employed to measure ^{1}H longitudinal relaxation times in the

H^{α} region. Acquisition parameters were set similarly to panel a. To optimize solvent suppression, presaturation was applied during both the t_r and t_{var} delays. Phase cycling scheme and selective-pulse shapes were as in Supplementary Fig. 5.

Supplementary Figure 7. **Kinetic scheme illustrating the major steps involved in photo-CIDNP**.

Supplementary Figure 8. Noise-level contour plots of 2D ^{1}H–^{13}C–correlation reference spectra. All the images in this figure are noise-level plots of the spectra in panels A – C of Figure 4. Specifically: **a** and **b,** these panels show noise-level reference spectra in two different $^{1}H^{\alpha}$ $^{13}C^{\alpha}$ regions. Note that the large direct-dimension spectral features of the ^{13}C PREPRINT dark spectra are due to tails of the residual solvent signal. These features were not observed in the reference ^{1}H-^{13}C CT-SE-HSQC spectra due to the different solvent-suppression schemes used in the ^{1}H-^{13}C CT-SE-HSQC and ^{13}C PREPRINT experiments. **c,** this panel shows noise-level reference spectra in the $^{1}H^{13}C$ aromatic region.

Supplementary Figure 9. 2D ^{13}C-PREPRINT analysis of the SH3 protein (20 µM, light spectrum). This 2D spectrum highlights the LC-photo-CIDNP-active resonances Y37 and Y52.

Supplementary Figures

Supplementary Figure 1

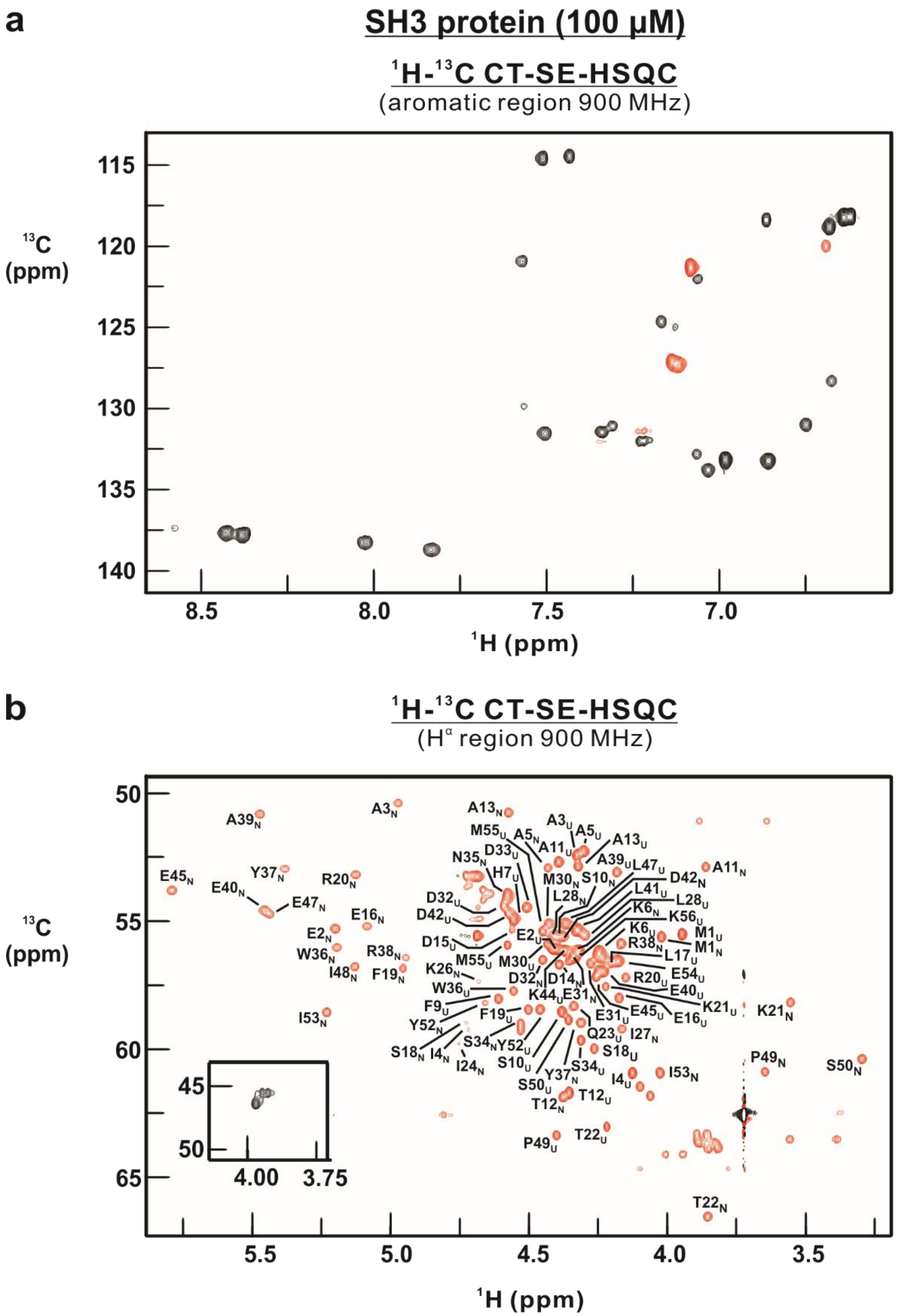

Supplementary Figure 2

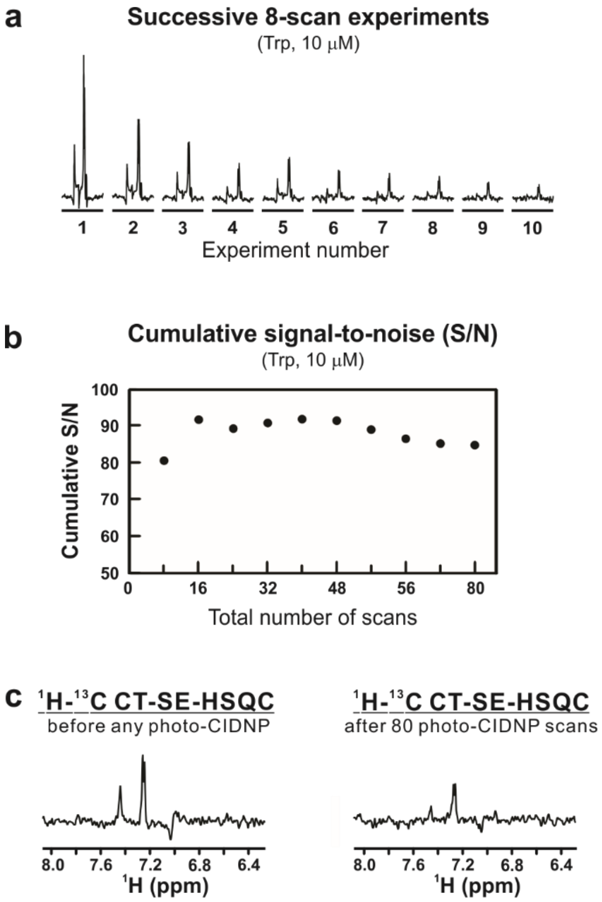

Supplementary Figure 3

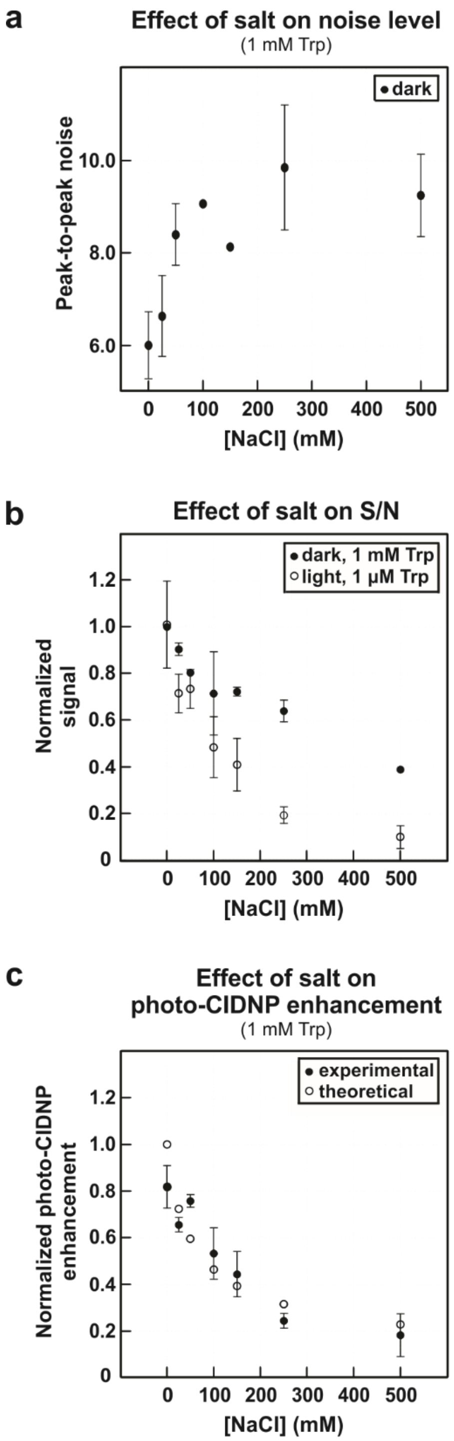

Supplementary Figure 4

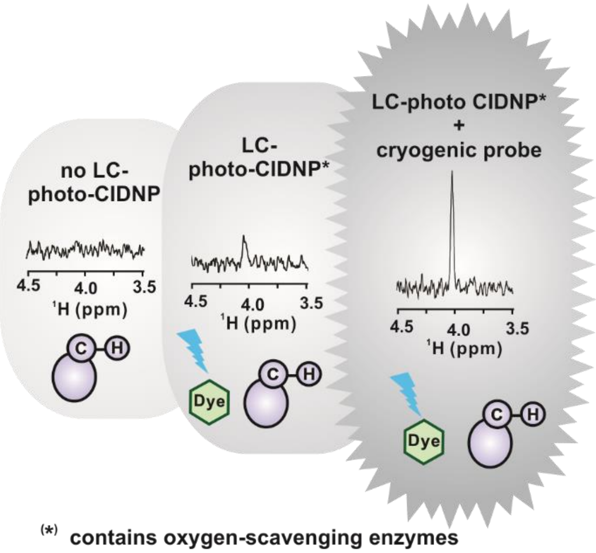

(*) contains oxygen-scavenging enzymes and a dye tailored to low concentration NMR samples

Supplementary Figure 5

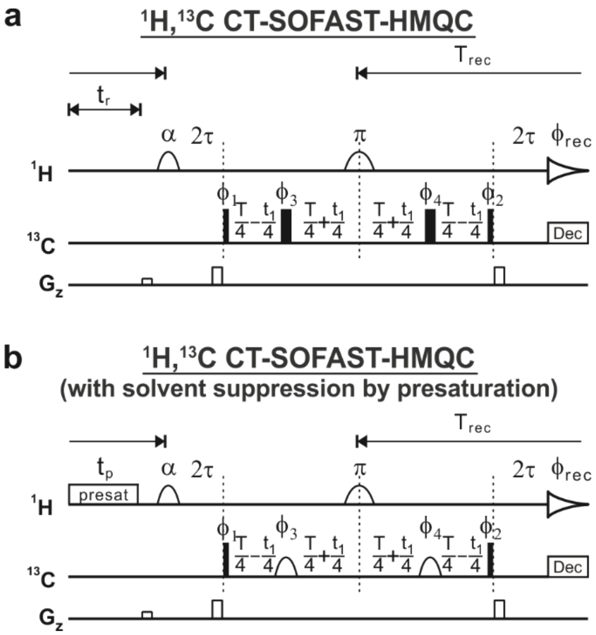

Supplementary Figure 6

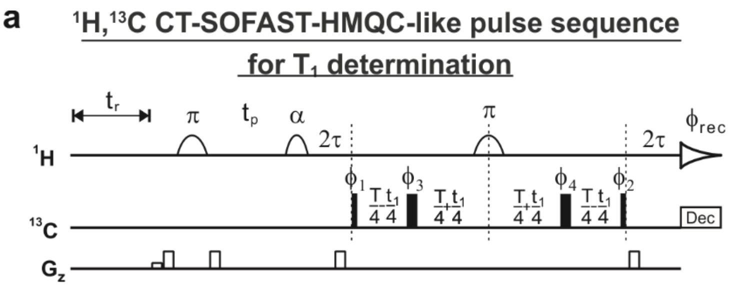

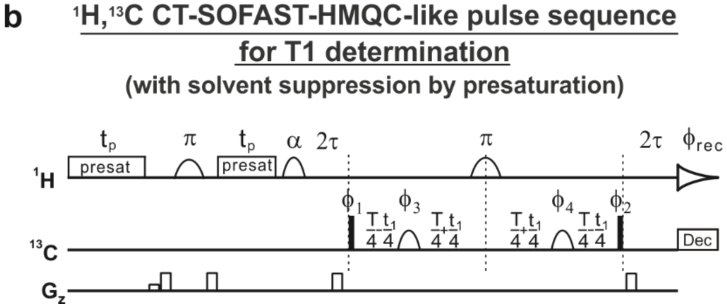

Supplementary Figure 7

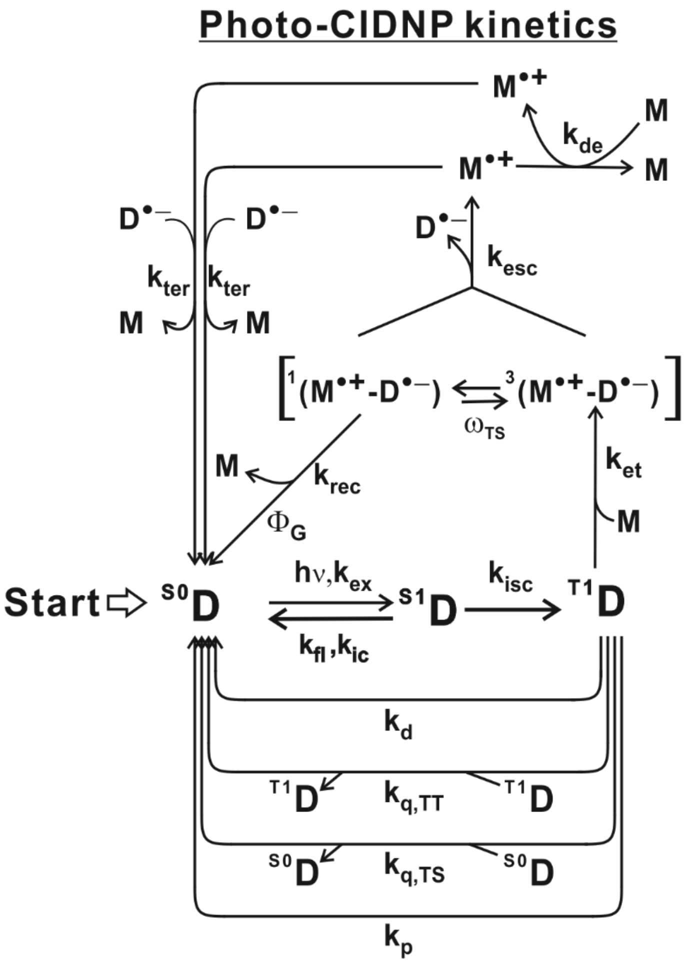

LEGEND

^{S0}D : ground-state dye
^{S1}D : singlet excited state dye
^{T1}D : triplet excited state dye
M : molecule of interest
$^{1}(M^{\bullet+}\text{-}D^{\bullet-})$: singlet radical pair
$^{3}(M^{\bullet+}\text{-}D^{\bullet-})$: triplet radical pair
ω_{TS} : triplet-singlet mixing frequency
Φ_G : probability of geminate recombination
k_{ex} : excitation rate constant
k_{fl} : singlet decay rate constant
k_{isc} : intersystem crossing rate constant
k_d : triplet-decay-rate constant
$k_{q,TT}$: triplet-triplet self quenching rate constant
$k_{q,TS}$: triplet-ground-state self-quenching rate constant
k_p : phosphorescence rate constant
k_{et} : electron transfer rate constant
k_{rec} : nuclear-spin-dependent recombination rate constant
k_{esc} : nuclear-spin-dependent escape rate constant
k_{ter} : nuclear-spin-dependent radical termination rate constant
k_{de} : rate constant for degenerate electron exchange between **M** and **$M^{\bullet+}$**

Supplementary Figure 8

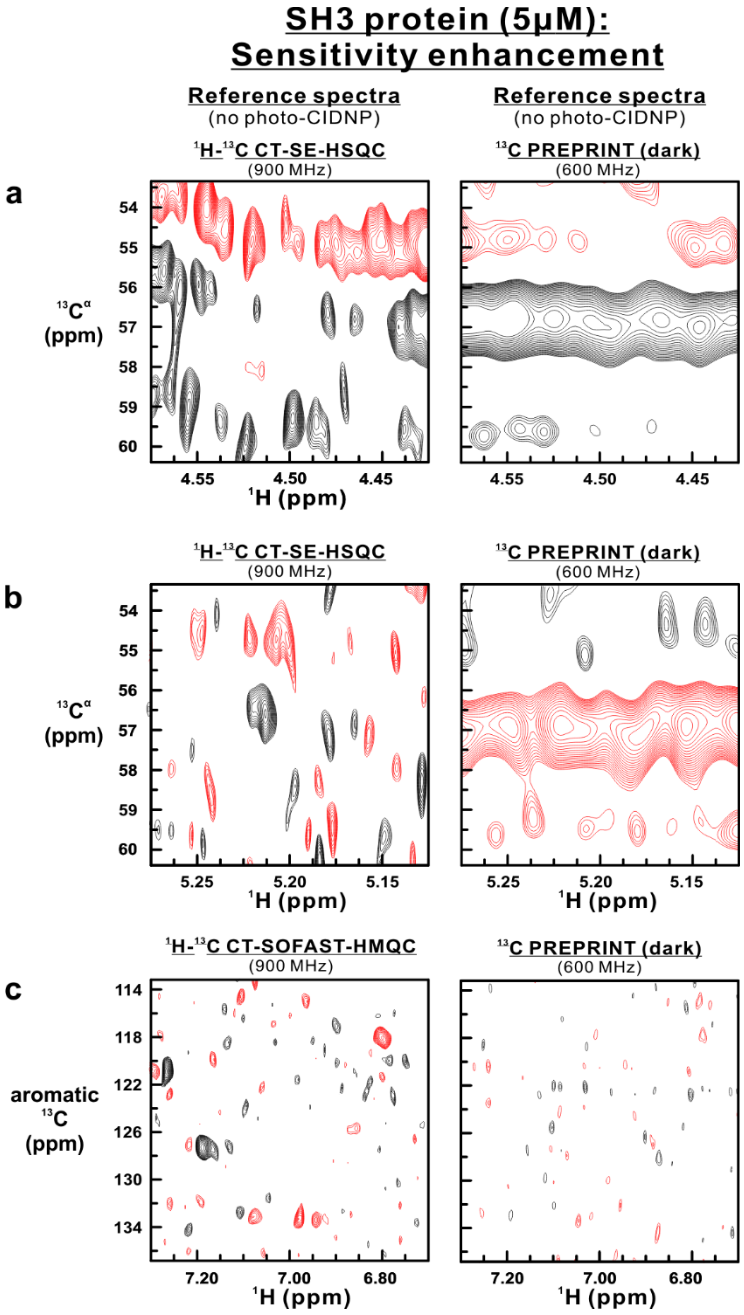

Supplementary Figure 9